BUTTERWORTH HEINEMANN

Heat transfer enhancement in a vertical channel with asymmetric isothermal walls by local blowing or suction

Yih Nen Jeng, Jiann Lin Chen, and Yeong-Ysong Chen
Institute of Aeronautics and Astronautics, National Cheng Kung University, Tainan, Taiwan, Republic of China

Win Aung
Department of Mechanical Engineering and Mechanics, Drexel University, Philadelphia, PA, USA

In this article, local heat transfer enhancement in a vertical parallel channel with asymmetric isothermal walls is numerically investigated. A porous wall segment is embedded in the hot wall to achieve this enhancement. By assuming the reference pressure and temperature on the other side of the hot wall, the heat transfer is enhanced as hot fluid is sucked from the channel. The heat transfer improvement is a local effect that becomes more effective with the increase of porosity and the distance measured from the entrance to the position of porous wall segment. It is shown that the local cooling enhancement is effective in low Reynolds number cases ($Re \leq 100$) but is less impressive when the Reynolds number is higher. The numerical results also show the possibility of embedding multiple porous segments in a single channel, provided that the mass fraction sucked out of the channel is limited.

Keywords: mixed convection; local heat transfer enhancement; segment of porous wall

Introduction

Mixed convection heat transfer between vertical parallel plates is important in conventional flat plate-type solar collectors and in equipment for electronics cooling. In the latter application, electronic components are normally mounted on parallel circuit boards positioned vertically in a cabinet and form vertical parallel channels through which coolants pass. The coolants may be propelled by free convection, forced convection, or mixed convection, depending on the power density of the circuit boards. The present physical model, therefore, is a parallel-plate channel with asymmetric wall temperatures in which steady heat transfer characteristics in laminar mixed convection are investigated. Such steady laminar mixed convection in a vertical plane channel has been extensively investigated by numerical (Tao 1960; Aung and Worku 1986a, 1986b; Ingham et al. 1988) and experimental methods (Aung et al. 1972; Sparrow et al. 1984).

On a printed circuit board (PCB), power supply devices and the central processing unit (CPU) may pose more of a heat transer problem than other components. To keep such units within the range of working temperature, designers have added external devices to serve as local heat transfer promoters. There are many external devices in the literature: the barriers of Sparrow et al. (1982), the vortex generators of Chou et al. (1988) and Lee and Huang (1988), and rods by Patera and Mikic (1980) and Ratts et al. (1988).

In general, surface temperatures on the two sides of a PCB are different because of the arrangement of electronic components. Consequently, the coolant temperature of a channel (or module formed by PCBs) on one side of a PCB may be higher than the coolant temperature on the other side. For the case where buoyancy aids the forced flow, we can effect mass transfer by drawing the hot air on one side of the PCB into the airstream on the other side (or vice versa) by drilling small holes through the PCB, which can be then approximated by a porous wall segment. Thus, hot fluid can be drawn from, or cold fluid can be forced into, the channel of concern. Of course, this potential heat transfer enhancement scheme can be achieved only if the pressure of the hotter side is higher (or lower) than that of the cooler side. The effect of the local heat transfer enhancement depends upon the difference between two sides of a PCB. If the pressure difference is large enough, the enhancement will be significant. As discussed later, this, indeed, is feasible under certain conditions.

The schematic diagram of a simplified model is shown in Figure 1. On the hot wall, a porous wall segment of length Δx_p is placed at a distance x_p measured from the inlet. Buoyant force may create an adverse pressure gradient, so that the pressure will increase along the streamwise direction. Therefore, the porous wall may have a suction effect and, hence, modify the local flow and the thermal fields.

In the present numerical study, we investigate the heat transfer enhancement through local blowing or suction at a porous wall segment. The parameters, position of the porous wall segment, permeability, and the Reynolds number are varied to explore some interesting results.

Physical model descriptions

Governing Equations

The nondimensional Navier–Stokes equations and the boundary conditions that describe the physical situation shown

Address reprint requests to Professor Jeng at the Institute of Aeronautics and Astronautics, National Cheng Kung University, 70101 Tainan, Taiwan, Republic of China.

Received 11 March 1994; accepted 1 August 1994

Int. J. Heat and Fluid Flow 16:25–35, 1995

655 Avenue of the Americas, New York, NY 10010

0142-727X/95/$10.00
SSDI 0142-727X(94)00004-V

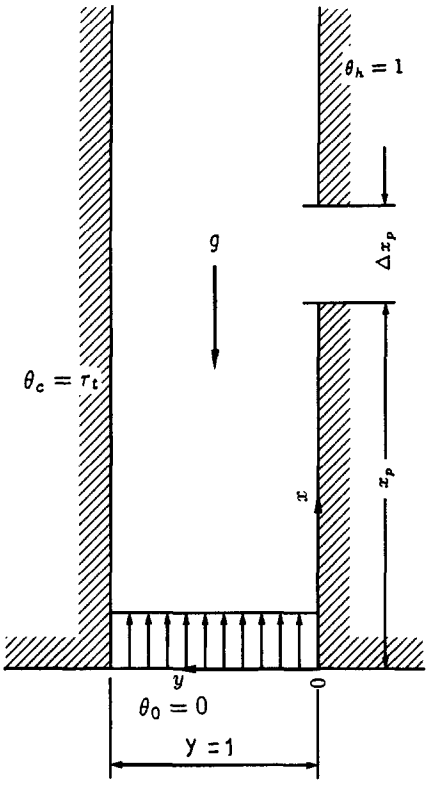

Figure 1 The physical model of mixed convection in a vertical channel embedded with a porous wall segment

in Figure 1 are written in the Cartesian coordinate system as follows:

$$\frac{\partial u}{\partial x} + \frac{\partial v}{\partial y} = 0 \tag{1}$$

$$u\frac{\partial u}{\partial x} + v\frac{\partial u}{\partial y} = -\frac{\partial p}{\partial x} + \frac{\mathrm{Gr}}{\mathrm{Re}^2}\theta + \frac{1}{\mathrm{Re}}\left(\frac{\partial^2 u}{\partial x^2} + \frac{\partial^2 u}{\partial y^2}\right) \tag{2}$$

$$u\frac{\partial v}{\partial x} + v\frac{\partial v}{\partial y} = -\frac{\partial p}{\partial y} + \frac{1}{\mathrm{Re}}\left(\frac{\partial^2 v}{\partial x^2} + \frac{\partial^2 v}{\partial y^2}\right) \tag{3}$$

$$u\frac{\partial \theta}{\partial x} + v\frac{\partial \theta}{\partial y} = \frac{1}{\mathrm{Re}\cdot\mathrm{Pr}}\left(\frac{\partial^2 \theta}{\partial x^2} + \frac{\partial^2 \theta}{\partial y^2}\right)$$

$x = 0, 0 \le y \le 1$: $u = 1$, $v = 0$, $\theta_o = 0$, $p = 1$

$x > 0, y = 0$: $u = 0$, $v = 0$, $\theta_h = 1$ for solid wall

: $u = 0, v = v_n < 0, \partial\theta/\partial y = 0$ for suction case

: $u = 0$, $v = v_n > 0$, $\theta_h = \theta_o$ for blowing case

$x > 0, y = 1$: $u = 0$, $v = 0$, $\theta_c = r_t$ (4)

where u and v are normalized by the inlet velocity u_o, x and y are normalized by the channel width b, pressure is normalized by the dynamic head ρu_o^2 at the inlet, and $\theta = (T - T_o)/(T_h - T_o)$. The Boussinesq approximation for the buoyant force term has been employed, and the Reynolds number, Grashof number, and Prandtl number are defined as $\mathrm{Re} = u_o b/\nu$, $\mathrm{Gr} = g\beta(T_h - T_o)b^3/\nu^2$, and $\mathrm{Pr} = \nu/\alpha = 0.72$, respectively. Moreover, to ensure the validity of uniform inlet condition for low Reynolds number cases, it is assumed that the leading edge of parallel plates were properly rounded or that a convergent channel was connected upstream of the parallel channel.

To reduce the complexity of the problem, Darcy's law is employed to model the flow across the porous wall. Without loss of generality, the pressure on the other side of the PCB is assumed to be the inlet pressure of the channel, so that a pressure difference between the two sides of the wall can be established. The Darcy law (Hartnett 1985; Payne 1978; Hamed and Lehnig 1990) for the present porous wall is written as follows:

$$v_n = c(p - 1) \tag{5}$$

in which c is the porosity factor; v_n is the dimensionless velocity component normal to the porous wall; p is the local dimensionless static pressure on the hot wall, and the unity value of pressure represents the prescribed uniform pressure on the other side of the hot wall. Following Payne (1978), the porosity factor is restricted to be no more than $O(1)$ so that it is within the interest of engineering applications.

Fully developed flow solution

Aung and Wonku (1986b) solved the fully developed flow of Figure 1 without the porous segment. They expressed the relation between Re, Gr, r_t, and dp/dx as follows:

$$\mathrm{Re}\frac{dp}{dx} = \frac{\mathrm{Gr}}{\mathrm{Re}}\frac{(1 + r_t)}{2} - 12 \tag{6}$$

Notation

b	channel width
c	porosity factor in Equation (5): $\gamma K \mathrm{u}_o, v\Delta y$
g	magnitude of the gravitational acceleration
K	permeability
k	thermal conductivity
L_s	location of separation point
$\dot{m}$	mass flow rate
Nu	local Nusselt number at hot wall, $\frac{1}{\theta_b}\frac{\partial\theta}{\partial y}\Big\vert_{y=1}$
$\overline{\mathrm{Nu}}$	local mean Nusselt number, Equation (7)
p	dimensionless local pressure
r_t	dimensionless temperature at cold wall
T	temperature
u, v	dimensionless velocities in x and y directions, respectively
x, y	dimensionless coordinates

Greek symbols

α	thermal diffusivity of air
β	coefficient of thermal expansion of air
γ, ρ	specific weight and density of air, respectively
θ	dimensionless temperature
ν	kinematic viscosity of air
Δy	thickness of porous plate
Ψ	stream function

Subscripts

b	bulk
c	cold wall ($y = 1$)
h	hot wall ($y = 0$)
o	entrance

Without the bouyant effect, the pressure will monotonically drop. As the buoyant effect is added, the fully developed flow solution indicates that the pressure drop becomes more and more moderate. Whenever the buoyant force is strong enough, the pressure is a positive value. For example, for Re = 100 and $r_t = 0.3$, the pressure gradient will become positive as Gr/Re $\geq$ 18.5. If Gr/Re = 100, the pressure gradient has a positive value of 27/Re. As discussed in the introductory section, two adjacent channels separated by a PCB may have different heating conditions. Consequently, a significant pressure difference may exist on the two sides of a PCB.

From the fully developed flow analysis, it seems that, if the channel height is large enough, introducing mass exchange through a porous segment embedded in the PCB is possible. In this study, a numerical procedure is employed to examine how the entrance of the channel affects the possibility of mass exchange.

Numerical methodology

Equations 1–4 can be formulated via the finite volume method for a general staggered grid system (Jeng and Chen 1992a; 1992b). The convective term was approximated by the classical second-order upwind scheme, and the diffusive used the central difference scheme, provided that the geometric conservation law was satisfied (Jeng and Chen 1992b). In numerical calculation, the inflow boundary conditions of Equation 5 are employed. For outflow boundary conditions, we use the first-order extrapolation of Shyy (1987). Generally speaking, the present problem is parabolic in nature, even when flow reversal occurs (Jeng et al. 1992). Therefore, the first-order extrapolation at the exit plane is reasonable. The SIMPLE algorithm is then employed to solve the resulting simultaneous algebraic equations (Jeng and Chen 1992b), and the inner loop iteration uses the successive line under relaxation iteration method. The calculation stops when all the maximum residues of mass momentum, and energy are less than 5×10^{-7}.

Results and discussion

Code validation

To check the validity of the program, a high Reynolds number, forced-convection flow between parallel flat plates, which was analytically solved by Heaton et al. (1964), is first considered. One wall is heated at uniform heat flux, and the other is adiabatic. The analytic solution is independent of the Reynolds number.

In the present study, numerical solutions are obtained for Reynolds numbers of 1000 (with 151 × 41 algebraic stretched grids) and 660 (with 121 × 41 algebraic stretched grids). The results are shown in Figure 2. The agreement between the exact solution and two numerical solutions (with streamwise coordinates being properly scaled) is obvious.

The second test problem uses the experimental data of Aung et al. (1972), where Gr/Re = 23.44 and $r_t = 0.33$. Figure 3 displays the local Nusselt numbers along the hot and cold walls. The quantity 2.2 in the streamwise coordinate in Figure 3 results from using different dimensionless groups between the present study and Aung et al., in which a characteristic channel length was employed. Numerical calculations are obtained for two different Reynolds numbers, and the two sets of results nearly coincide with each other. As is shown, both numerical results are close to the experimental data.

The third test problem is the driven cavity flow with Re = 1000 (Ghia et al. 1982) using 80 × 80 and 129 × 129 uniform grid systems. Figure 4 compares the present result and vorticity–stream function solution of Ghia et al. along centerlines of the cavity. The coarse grid solution deviates slightly from the Ghia et al. result, while the fine grid solution coincides to their solution within drawing error.

The above test cases show that the results of the present code agree very well with the exact solution of the limiting case, the experimental results, and the existing numerical solution. This gives us confidence to proceed.

Entrance effect of the nonporous wall

Consider the following conditions. The hot wall temperature of the channel is $\theta_h = 1$, the cold wall temperature is $\theta_c = r_t = 0.3$, and the inlet temperature is $\theta_o = 0$. For convenience, assume that the conditions on the other side of the PCB are $p/p_o = 1$ and $\theta = 0$.

In our previous study (Jeng et al. 1992), we found that the flow field described by the above conditions without the porous wall segment have similar property (independent of the

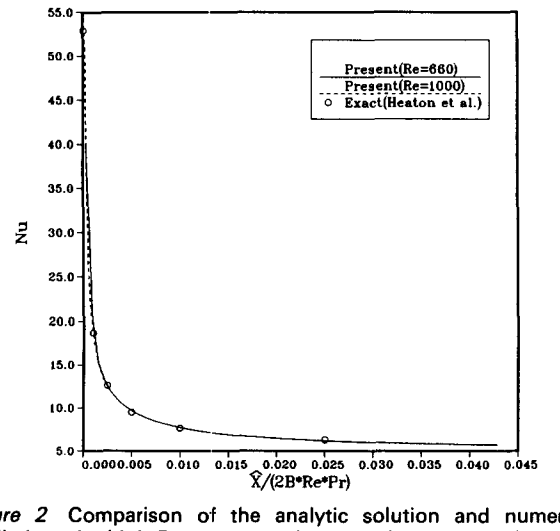

Figure 2 Comparison of the analytic solution and numerical prediction of a high Reynolds number forced convection flow

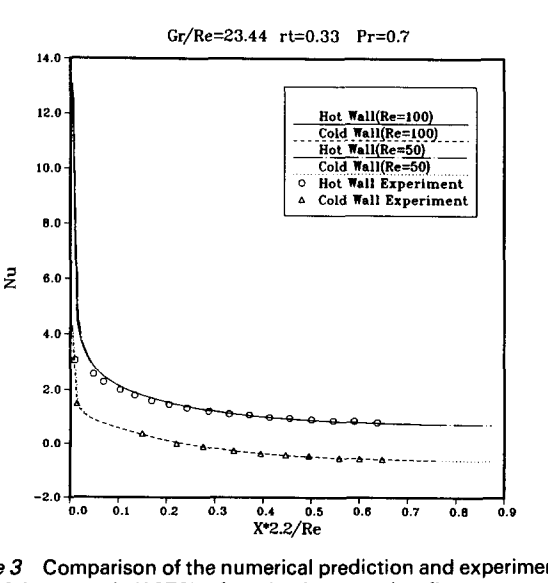

Figure 3 Comparison of the numerical prediction and experimental data of Aung et al. (1972) of a mixed convection flow

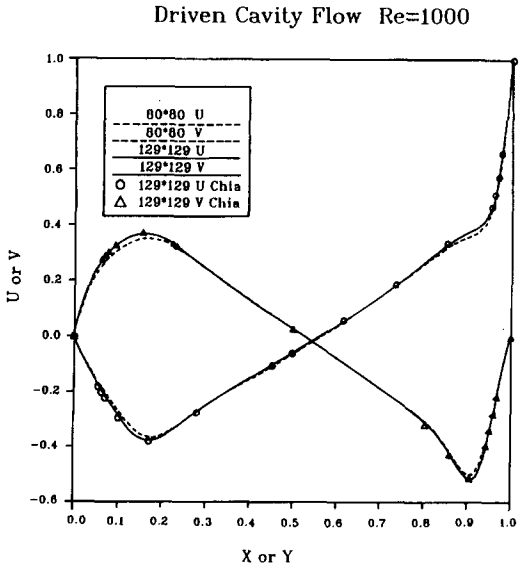

Figure 4 Comparison of velocity distributions along centerlines of the driven cavity flow

Reynolds number) even in the presence of flow reversal in the situation where $50 \leq Re \leq 1000$ and $0 \leq Gr/Re \leq 500$. Therefore, we consider Gr/Re to be a parameter rather than Gr/Re^2 shown in Equation 2. In Figures 5(a–c), several pressure distributions of different Gr/Re along the hot wall are shown for Re = 50, 100, and 500. These graphs show that the pressure decreases near the inlet and then may or may not increase. In a cold channel flow where Gr/Re = 0, the pressure decreases monotonically along the channel. However, after the walls are heated, a buoyant force is imposed, and the pressure distribution changes. The pressure is first dominated by viscous losses. As the fluid moves forward, the viscous force is gradually counterbalanced by the buoyant force. If the channel is long enough and Gr is large enough, the buoyant force not only compensates the viscous force but also provides an upward driving force (as in the case of a natural convective flow) that changes the pressure to a positive value. Eventually, if the channel height is tall enough, the pressure will approach that predicted by Equation 6.

The degree of compensation at the entrance region depends on the parameters Re and Gr/Re, whose relation is shown in Equation 2. In this equation, the magnitude of the viscous force is represented by 1/Re, while that of the buoyant force is represented by Gr/Re^2. As the Reynolds number becomes larger, for a fixed value of Gr, the attenuation of the buoyant force's effect is faster than that of the viscous force. Therefore, as shown in Figures 5(a–c), in the lowest Reynolds number case where Re = 50, the pressure turns out to be greater than 1 for $Gr/Re \geq 40$ at the location $x \geq 8$, while in the largest Reynolds number case where Re = 500, the pressure never becomes positive in the region $x < 14$ for all the examined values of Gr/Re.

A careful examination of Figures 5(a–c) reveals that the present idea of heat transfer enhancement via a porous segment embedded in the hot wall works only for cases with low Reynolds numbers. Note that the length of a PCB is generally of order $x = 10$, which is too short to reach the fully developed region except when the Reynolds number is very small. This fact also demonstrates that the prediction of the possibility of embedding a porous segment to enhance heat transfer via Equation 6 can work only when the Reynolds number is small.

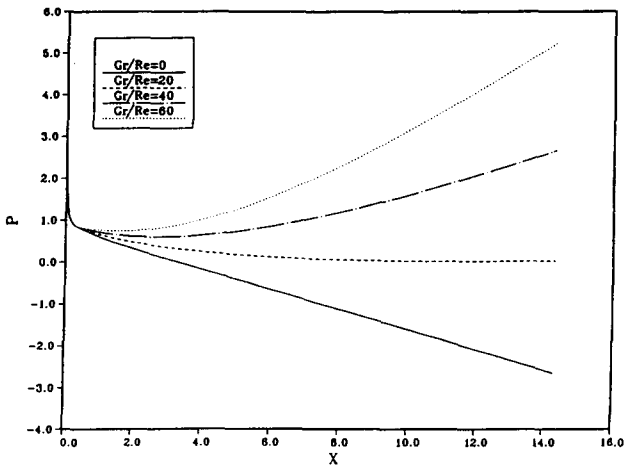

Figure 5(a) The pressure distribution of different Gr/Re along the hot wall, Re = 50

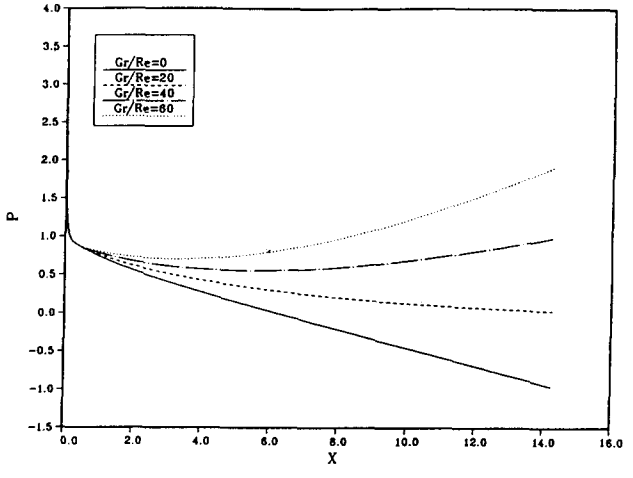

Figure 5(b) The pressure distribution of different Gr/Re along the hot wall, Re = 100

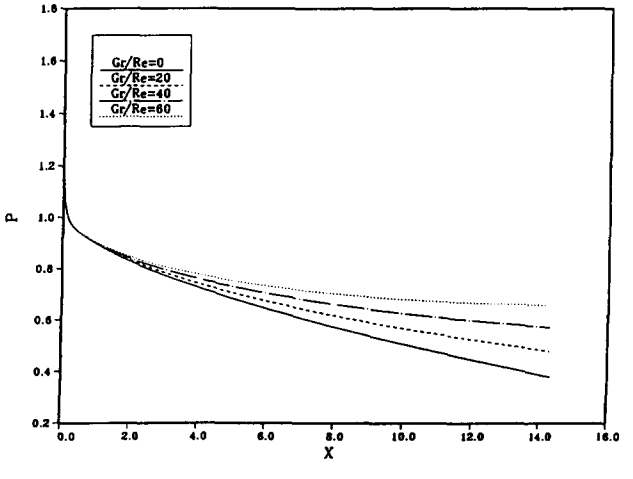

Figure 5(c) The pressure distribution of different Gr/Re along the hot wall, Re = 500

Grid independence

In this section, the case where Gr/Re = 300, Re = 100, $r_t = 0.3$, and $c = 0.2$, with a porous plate of lengh $\Delta x = 0.1$ embedded at $x_p = 8$, is examined to looking for a suitable grid density. During the calculation, if the fluid is blown into the channel, the fluid temperature is assumed to be $\theta = \theta_o = 0$. On the other hand, if fluid is sucked out from the channel, all the fluid properties are approximated by the zero order extrapolation approximation (Hamed and Lehnig 1990).

Note that this specific flowfield can be solved through the Cartesian grid system. However, a rectangular grid system requires a very fine grid system to reach grid-independent resolution. Moreover, our test runs showed that the necessary CPU time for a single run will be 10 times longer than that employing a generalized grid system with proper grid clustering around the suction slot. Therefore, we use the generalized grid system generated by the elliptic generation method in Thomas and Middlecoff (1980).

After several test runs, the grid system shown in Figures 6(a) and 6(b) (121 × 31 points) is chosen. The streamline and isothermal contours obtained on the grid system are shown in Figures 7(a) and 7(b), respectively. These solutions have been compared with those on fine algebraic stretching grids (151 × 41) and coarse generalized grids (61 × 21). The Nusselt number distributions along the hot wall and the bulk temperature distribution along the x-direction are shown in Figures 8(a) and 8(b), respectively, for three different grid systems. These comparisons reveal that the typical generalized grid system (121 × 31) reaches grid independence. For cases with single suction slots with different locations of x_p and multiple suction slots, grid systems use the grid density around the slot similar to that of Figure 6(b).

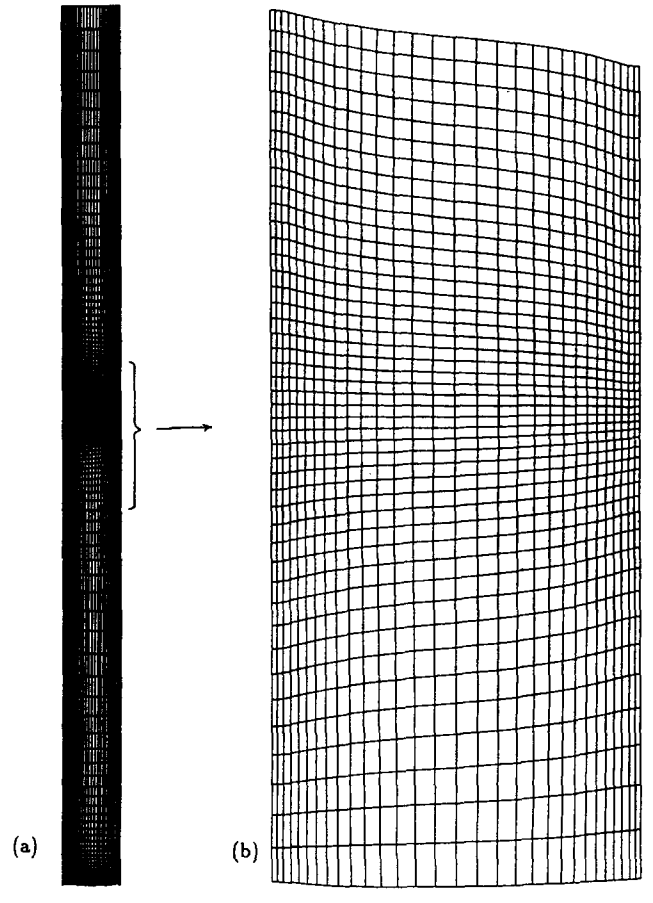

Figure 6(a) The generalized grid system (121 × 31 points)
Figure 6(b) The detailed grid distribution around the porous wall region

Channel embedded in hot wall by a porous wall segment

Now let us look into the physics of Figures 7 and 8. Because the mean pressure over the porous wall is about 4.32, which is significantly larger than the prescribed pressure on the other side ($p_o = 1$), the suction flow is induced as shown by the streamline contours of Figure 7(a). By examining the value of the stream function at $y = 1$ and x as slightly larger than $x_p + \Delta x_p$, it is found that the resulting suction mass flow rate ($= v_n \Delta x_p$) is 6.63 percent of the inlet mass flow rate, which corresponds to a relatively large $v_n = 0.663$. Because the total mass in the channel is reduced, and the hot fluid adjacent to the hot wall is removed, the bulk temperature also decreases at the downstream side, as shown in Figure 8(b).

In Figure 7(a), there is a region of flow reversal enclosed by the boundaries and separation line where $\Phi = 0$. As shown in Table 1, the separation point is nearly independent of the presence of the porous wall segment. Because of the flow reversal and zero-gradient open boundary conditions (Shyy 1987; Jeng et al. 1992), the isotherm has a line of bifurcation starting from the separation point, as shown in Figure 7(b).

The hot suction stream across the porous segment induces a stream of cold fluid (originally in the interior region) impinging on the downstream part of the porous segment. Such a phenomenon is similar to a wall jet flow. Consequently, both the momentum and thermal boundary layer thicknesses suddenly become thin. The local heat transfer enhancement is

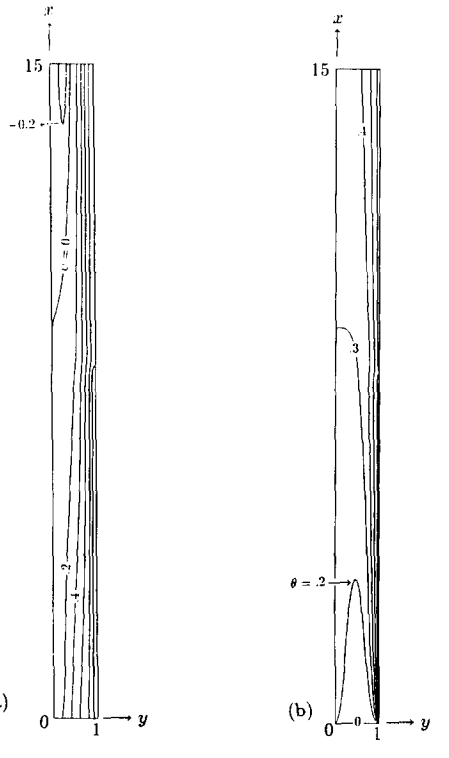

Figure 7(a) The streamline contours of the case where Gr/Re = 300, Re = 100, $c = 0.2$, $r_t = 0.3$, $x_p = 8$
Figure 7(b) The isothermal contours of the case where Gr/Re = 300, Re = 100, $c = 0.2$, $r_t = 0.3$, $x_p = 8$

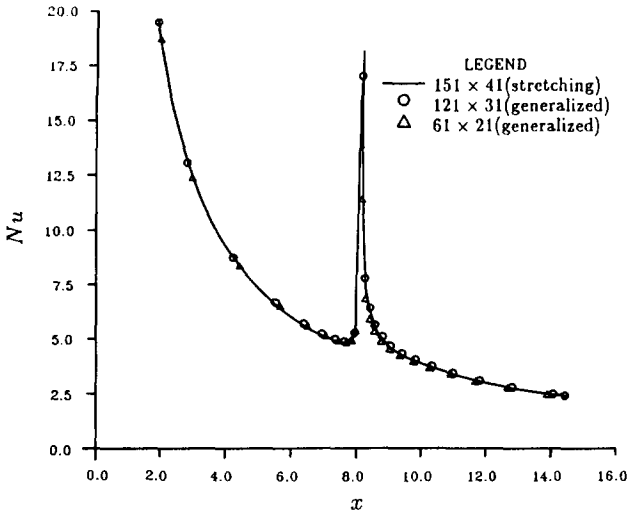

Figure 8(a) The Nu distributions (along the hot wall) against x of cases with and without single porous wall segment on three different grid systems; Gr/Re = 300, Re = 100, $c = 0.2$, $r_t = 0.3$, $x_p = 8$

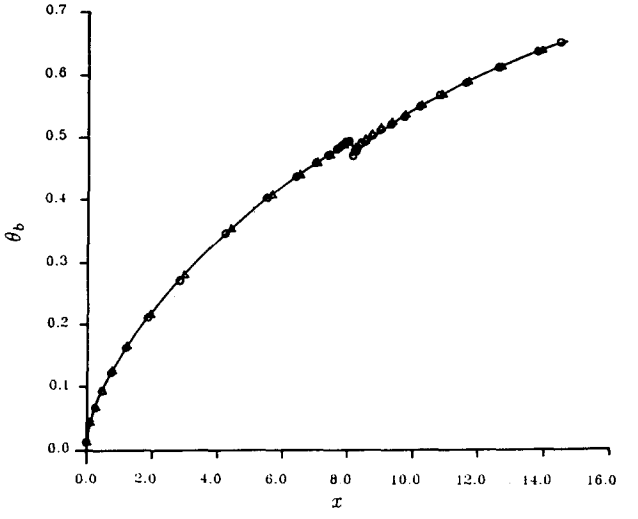

Figure 8(b) The θ_b distributions against x of cases with and without single porous wall segment on three different grid systems; Gr/Re = 300, Re = 100, $c = 0.2$, $r_t = 0.3$, $x_p = 8$

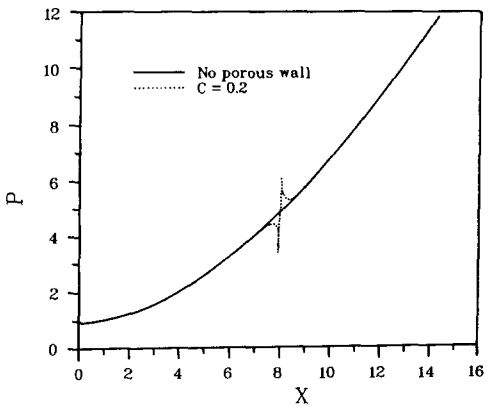

Figure 8(c) The pressure distribution (along the hot wall) against x of cases with and without single porous wall segment, using the grid system of Figure 4(a); Gr/Rd = 300, Re = 100, $c = 0.2$, r_t0.3, $x_p = 8$

Table 1 Results of aiding flow with a porous wall segment with $\Delta x_p = 0.1$, Re = 100, Gr/Re = 300, and $r_t = 0.3$*

	Parameters	$x_p = 4$	$x_p = 8$	$x_p = 12$
	$\bar{v}$	0.0245	0.0950	0.1961
	$\dot{m}$	0.9975	0.9905	0.9804
$c = 0.025$	$\bar{p}$	1.9802	4.8006	8.8445
	$\bar{\theta}$	0.9025	0.9126	0.9386
	L_s	9.1797	9.1502	9.1717
	$\bar{v}$	0.0485	0.1874	0.3846
	$\dot{m}$	0.9951	0.9813	0.9615
$c = 0.05$	$\bar{p}$	1.9702	4.7485	8.6921
	$\bar{\theta}$	0.9007	0.9069	0.9310
	L_s	9.1768	9.1322	9.1706
	$\bar{v}$	0.0946	0.3623	0.7315
	$\dot{m}$	0.9905	0.9638	0.9268
$c = 0.1$	$\bar{p}$	1.9463	4.6233	8.3153
	$\bar{\theta}$	0.8973	0.8966	0.9179
	L_s	9.1725	9.0983	9.1713
	$\bar{v}$	0.1787	0.6632	1.2817
	$\dot{m}$	0.9821	0.9337	0.8718
$c = 0.02$	$\bar{p}$	1.8936	4.3159	7.4086
	$\bar{\theta}$	0.8911	0.8804	0.9005
	L_s	9.1614	9.0405	9.1711
	Parameters	$x_p = 4$	$x_p = 8$	$x_p = 12$
	$\bar{v}$	0.2165	0.7871	1.4864
	$\dot{m}$	0.9783	0.9212	0.8513
$c = 0.02$	$\bar{p}$	1.8661	4.1484	6.9457
	$\bar{\theta}$	0.8884	0.8746	0.8949
	L_s	9.1546	9.0150	9.1712
	$\bar{v}$	0.2732	0.9579	1.7465
	$\dot{m}$	0.9272	0.9042	0.8253
$c = 0.333$	$\bar{p}$	1.8196	3.8736	6.2396
	$\bar{\theta}$	0.8845	0.8673	0.8885
	L_s	9.1460	8.9825	9.1723
	$\bar{v}$	0.3653	†	†
	$\dot{m}$	0.9635	†	†
$c = 0.5$	$\bar{p}$	1.7305	†	†
	$\bar{\theta}$	0.8784	†	†
	L_s	9.1321	†	†

* The separation location L_s without porous wall is 9.1612
† No solution obtained.

achieved in a manner somewhat like the heat transfer characteristics at the entrance [see Figure 7(a)]. It is noted that the present numerical procedure assumes that all the numerical properties (p and θ) on the porous wall are extrapolated from interior grid points. Hence, conductive heat transfer on the porous wall is not encountered ($\partial\theta/\partial y = 0$ is assumed at porous wall segment). Although this simplification may induce error, the resulting heat transfer is only slightly underestimated and does not influence the characteristic of the heat transfer enhancement.

In Figure 8(c), the pressure distributions with and without the porous plate along the hot wall are shown. It is seen that, except at regions around the porous plate, the pressure distribution is negligibly influenced by fluid suction. Because the streamline next to the hot wall approaches the wall in the region ahead of the porous region [see Figure 5(a)], indicating a local flow acceleration, the pressure is reduced and attains a local minimum value. At the downstream side, the suction stream induces a stream from the interior region impinging upon the wall. Consequently, one part of the kinetic energy is

converted into static pressure so that the pressure is suddenly increased.

The fact that the embedding of the porous plate has little influence on the original pressure distribution along the hot wall indicates the possibility of employing the numerical result of the solid wall case as a first estimation for determining the location for embedding the porous segment. From this point of view and Figure 8(c), it is clear that a location close to the exit boundary is a better choice, because the pressure at the exit is larger than that at the other regions. In the next paragraph, this point is verified by examining the effect of x_p.

In Figure 9, the local Nusselt number of distributions of three different porous wall arrangements, $x_p = 4$, 8, and 12, are plotted together, while the corresponding bulk temperature and pressure distributions are shown in Figures 10 and 11, respectively. Again, all the local Nu distributions around the porous wall downstream are significantly improved, and the bulk temperatures decrease at locations downstream of the embedded porous segment. Because a greater pressure will build up in the interior part of the channel as the porous segment is embedded farther downstream, the volume of removed fluid will be larger. Therefore, the local heat transfer improvement, the decrease of the bulk temperature distribution, and the pressure variation around the porous segment become more and more obvious as the embedding location moves in the downstream direction, as shown. Note that the pressure distribution is still not significantly affected except at those regions around the porous segment.

Table 1 shows the means suction velocity, pressure, and bulk temperature over the range of the porous wall segment for three different locations of the porous wall segment and various permeabilities. Also shown is the mass flow rate at the exit plane, which is equal to $1 - 0.1\bar{v}$, and the variation of the separation point. Roughly speaking, the mean pressure $\bar{p}$ increases as x_p increases, while the mean velocity $\bar{v}$ increases as x_p or c increases.

Table 1 demonstrates that only a small fraction of fluid is sucked out, which explains why the flow and thermal fields near the cold wall are not significantly affected by the wall suction, as shown in Figures 7(a) and 7(b). For the same reason, the point of separation is nearly invariant; the original separation point is at $x = 9.16$, while that of the suction case is $x = 9.04$.

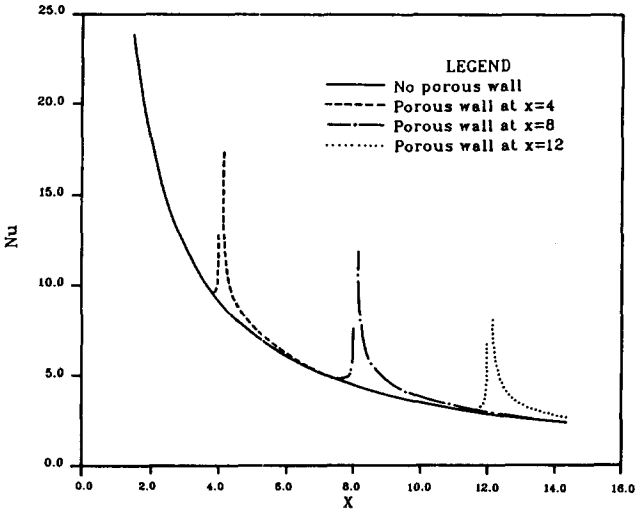

Figure 9 The Nu distribution (along the hot wall) for three different porous wall arrangements, $x_p = 4$, 8, or 12, and Gr/Re = 300, Re = 100, $c = 0.2$, $r_t = 0.3$, $x_p = 8$

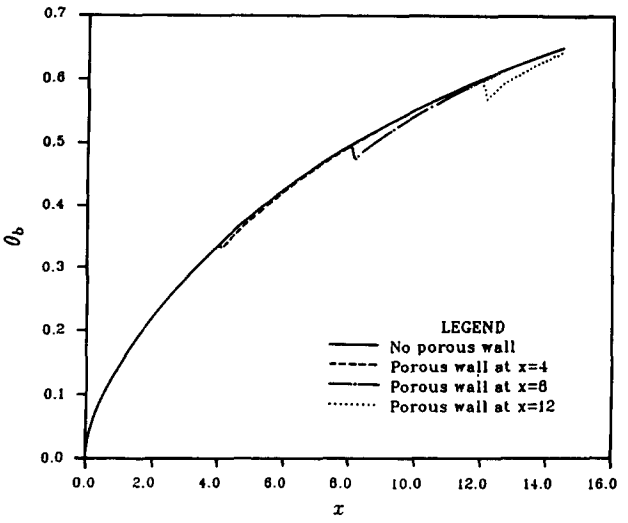

Figure 10 The θ_b distribution (along the hot wall) for three different porous wall arrangements, $x_p = 4$, 8, or 12, and Gr/Re = 300, Re = 100, $c = 0.2$, $r_t = 0.3$, $x_p = 8$

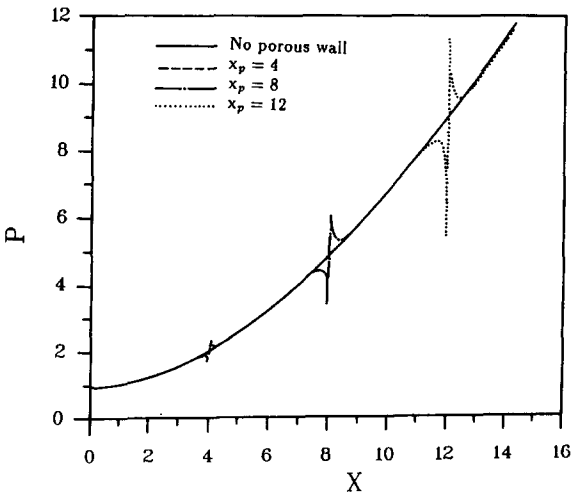

Figure 11 The pressure distribution (along the hot wall) for three different porous wall arrangements, $x_p = 4$, 8, or 12, and Gr/Re = 300, Re = 100, $c = 0.2$, $r_t = 0.3$, $x_p = 8$

Effects of permeability c

Generally, by virtue of the Darcy law of Equation 5, a larger c corresponds to a larger $\bar{v}$, as shown in Table 1. For a large enough c, however, the local wall suction velocity induces a large variation in fluid properties so that the computation becomes unstable. According to the numerical computations, the case where $x_p = 4$ cannot converge for $c \geq 1$, while for the cases where $x_p = 8$ and 12, the limitation for both is $c \geq 0.5$.

Consider first the cases with the same x_p. For a small permeability ($c = 0.05$), only the fluid near the hot wall is sucked out. For a larger permeability, on the other hand, which corresponds to a larger suction, coolant with a lower temperature is also sucked out. Consequently, the resulting bulk temperature for fluid remaining in the channel is lower than that for a smaller permeability.

For the situation where c remains constant, things become a little complicated. It is interesting to note that a larger x_p corresponds to a larger amount of thermal energy transferred from the hot wall to the fluid and larger suction because of a larger pressure difference between two sides of the porous wall segment. The former tends to increase the value of $\bar{\theta}$, while the latter makes it decrease. For a small value of c ($c = 0.05$ or 0.025), the suction is small, and the first factor dominates the second. Therefore, the mean temperature $\bar{\theta}$ of the sucked fluid increases with respect to increasing x_p, as shown in Table 1. For a larger permeability ($c \geq 0.1$), the balancing of these two opposite effects leads to the smallest value of $\bar{\theta}$ for cases where $x_p = 8$. Table 1 also shows that the mean pressure at a given x_p decreases with an increase in c and suction speed.

The effects of varying c on the local heat transfer enhancement are shown in Figure 12 (local Nusselt number) and Figure 13 (bulk temperature). Obviously, a larger c corresponds to a better local heat transfer enhancement, which is caused by a larger stream of cold fluid impinging on the wall. For a very small permeability ($c = 0.025$), the enhancement is still present. The modifications for the bulk temperature distributions for various porosity factors (c) are not obvious because the mass fraction sucked out of the channel is relatively small. However, we can still find the effect resulting from different porosity factors. It is worth pointing out that a larger c corresponds to a bigger hole or a higher density of holes, which may be impossible to implement on a PCB, because it might cause a structural problem.

From previous results, there is no doubt that the heat transfer enhancement is only a local phenomenon. We now attempt to identify the effective region at the downstream side of the embedded porous wall. In practical applications, this information could provide a guide to designers for the placement of high-power electronic components and CPU.

To check the effective region, we compare the improvement of the mean Nusselt number with respect to that of the solid wall case over five different ranges so that $x_f - x'$ is 0.5 1, 2, 3, and 4, where x' is the end location of the porous wall, and x_f is the end of integration. The local mean Nusselt number and the improvement are defined as follows:

$$\overline{\mathrm{Nu}} = \int_{x'}^{x_f} \mathrm{Nu}(x)\, dx/(x_f - x') \tag{7}$$

$$E_{\mathrm{Nu}} = (\overline{\mathrm{Nu}} - \overline{\mathrm{Nu}}^*)/\overline{\mathrm{Nu}}^*, \tag{8}$$

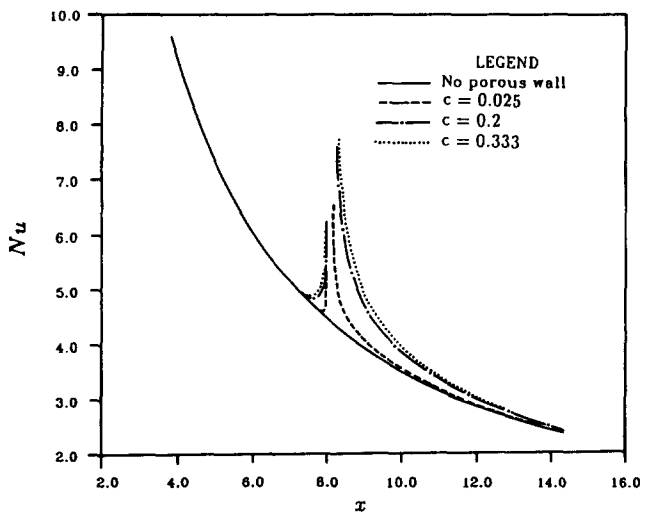

Figure 12 The Nu distributions against x of various c for the case with and without single porous wall segment at $x_p = 8$

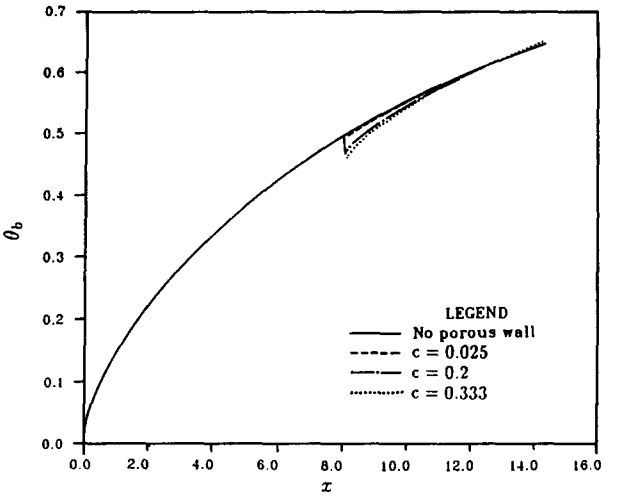

Figure 13 The θ_b distributions against x of various c for the cases with and without single porous wall segment at $x_p = 8$

where $\overline{\mathrm{Nu}}^*$ is the local mean Nusselt number of a nonporous wall.

Tables 2(a), 2(b), and 2(c) display the results for a single embedded porous wall segments in different channels (at $x_p = 4$, 8, and 12, respectively). Note that the case where $x_f - x' = 4$ in Table 2(c) is not included because of the limited computational domain. From these tables, we can see that the heat transfer improvement (E_{Nu}) is effective even for those cases with the largest range where $x_f - x' = 4$. Among the typical cases where $x_p = 8$ in Table 2(b), the most effective case is the one where $c = 0.333$, as expected. It is noteworthy that, for these conditions, the increment of the mean Nusselt number is about 92 percent for $x_f - x' = 0.5$. For the case where $x_f - x' = 4$, the improvement is still about 27 percent. For convenience, these values of E_{Nu} are represented by the following empirical relations

$$E_{\mathrm{Nu}} = (-56.3 + 22.4x_p)c^{0.336 + 0.036x_p}(x_f - x')^A$$
$$A = -(0.53 + 0.0053x_p)c^{0.082 - 0.005x_p} \tag{9}$$

which demonstrates that the improvement increases as c and x_p increase, but decreases with the increase of $x_f - x'$. Note that the relative heat transfer improvement E_{Nu} is evaluated based on $\overline{\mathrm{Nu}}^*$, which becomes smaller for values of x_f further downstream (see the last row in each table). The empirical relation shows that the improvement becomes more and more impressive as the porous wall segment is embedded further downstream. Therefore, the case where $x_p = 12$ has the largest heat transfer improvement. Table 2 also lists the mean wall pressure of the porous segment for various porosity factors (c) so that we can obtain the information according to pressure difference $p - 1$.

Because Tables 2(a–c) show that the case $x_f - x' = 0.5$ gives the best heat transfer improvement, a power unit or CPU should be placed next to the downstream side of the porous wall segment. Moreover, such devices should be near the upper part of the PCB because of the effect of x_p, as shown.

Arrangement of multiple porous wall segments and effect of Reynolds number

The above analysis illustrates that an embedded porous plate provides locally improved heat transfer behavior. Moreover, the mass fraction sucked out of the channel is rather small for the cases where $x_p = 4$ and 8. As a consequence, it is intuitively

Table 2(a) Heat transfer improvements of embedding a porous wall at $x_p = 4$ for various c

		$x_f - x'$ ($x' = 4.1$)					
c		0.5	1.0	2.0	3.0	4.0	$\bar{p}$
0.025	E_{Nu}	11.78%	7.19%	3.81%	3.41%	2.83%	1.9802
0.05	E_{Nu}	13.62%	8.52%	4.60%	4.15%	3.46%	1.9702
0.1	E_{Nu}	17.26%	11.15%	6.18%	5.62%	4.72%	1.9463
0.2	E_{Nu}	23.97%	15.95%	9.01%	8.26%	6.96%	1.8936
0.25	E_{Nu}	27.02%	18.10%	10.27%	9.43%	7.93%	1.8661
0.333	E_{Nu}	31.65%	21.37%	12.19%	11.21%	9.44%	1.8195
0.5	E_{Nu}	39.26%	26.73%	15.32%	14.10%	11.88%	1.7305
0.0	$\overline{Nu}^*$	8.4416	8.0073	7.2545	6.6874	6.2181	

Table 2(b) Heat transfer improvements of embedding a porous wall at $x_p = 8$ for various c

		$x_f - x'$ ($x' = 8.1$)					
c		0.5	1.0	2.0	3.0	4.0	$\bar{p}$
0.025	E_{Nu}	18.38%	11.75%	6.63%	5.66%	4.68%	4.8006
0.05	E_{Nu}	25.99%	17.22%	10.16%	8.63%	7.16%	4.7485
0.1	E_{Nu}	40.57%	27.58%	16.58%	14.18%	11.83%	4.6233
0.2	E_{Nu}	66.06%	45.38%	27.44%	23.50%	19.60%	4.3159
0.25	E_{Nu}	76.79%	52.72%	31.87%	27.27%	22.71%	4.1484
0.333	E_{Nu}	91.70%	62.91%	37.96%	32.44%	27.00%	3.8736
0.0	$\overline{Nu}^*$	4.2778	4.1425	3.9349	3.7190	3.5434	

Table 2(c) Heat transfer improvements of embedding a porous wall at $x_p = 12$ for various c

		$x_f - x'$ ($x' = 12.1$)				
c		0.5	1.0	2.0	3.0	$\bar{p}$
0.025	E_{Nu}	23.53%	15.68%	9.53%	7.17%	8.8445
0.05	E_{Nu}	37.36%	25.61%	15.88%	12.18%	8.6921
0.1	E_{Nu}	62.99%	43.74%	27.35%	21.14%	8.3153
0.2	E_{Nu}	104.28%	72.23%	45.06%	34.68%	7.4086
0.25	E_{Nu}	119.84%	82.78%	51.53%	39.57%	6.9457
0.333	E_{Nu}	139.98%	96.31%	59.75%	45.67%	6.2396
0.0	$\overline{Nu}^*$	2.7784	2.7215	2.6321	2.55014	

advantageous to consider more than one embedded porous wall segment. Results for a typical example of three simultaneous porous segments in a single channel (at $x_p = 4$, 8, and 12, with $c = 0.2$) are given in Table 3 for various Reynolds numbers. Figure 14 illustrates the case where Re = 100. The result shown in Figure 14 is attractive and similar to that of Figure 9.

Table 3 shows a mean suction velocity, pressure, and temperature for each porous region. The trend for each porous wall segment is nearly the same as those shown in Table 1 (the case where $c = 0.2$). The last column shows that nearly 22 percent of the inflow mass is sucked out (for Re = 100), which suggests less effective cooling downstream. In real applications, we can eliminate this drawback by limiting the length of a PCB to be no longer than 15 times the channel width.

The effect of Reynolds number is examined for the cases where Re = 100, 300, 500, and 1000, with $c = 0.2$. Because a large Re means that the growth of the thermal boundary-layer thickness is slower, the increase in the buoyant force is smaller. Consequently, the increase in pressure along the wall will be less and less significant with increase of Re, as shown in

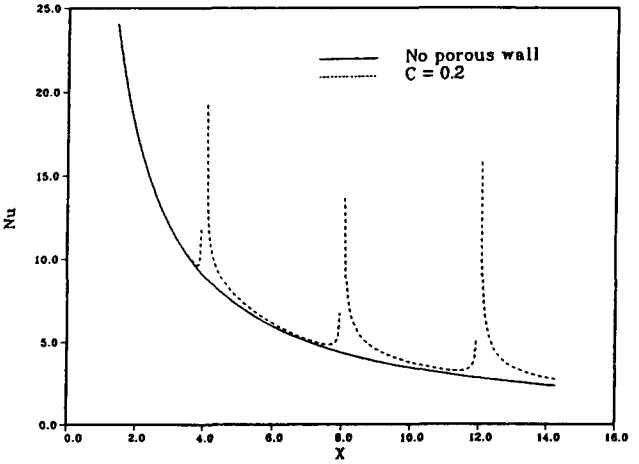

Figure 14 The Nu distribution (along the hot wall) for the case where three porous wall segments are embedded in a single channel, $x_p = 4$, 8, and 12; Gr/Re = 300, Re = 100, $c = 0.2$, $r_t = 0.3$, $x_p = 8$

Table 3 Results of aiding flow with three porous wall segments at $x_p = 4$, 8, and 12, respectively, with $\Delta x_p = 0.1$, $c = 0.2$, Gr/Re = 300, and $r_t = 0.3$

	Parameters	$x_p = 4$	$x_p = 8$	$x_p = 12$	Total $\dot{m}$
	$\bar{v}$	0.1761	0.6506	1.2886	
Re = 100	$\bar{p}$	1.8804	4.2531	7.4430	0.7885
	$\bar{\theta}$	0.8749	0.8829	0.8855	
	$\bar{v}$	0.0034	0.0699	0.1775	
Re = 300	$\bar{p}$	1.01668	1.3494	1.8874	0.9749
	$\bar{\theta}$	0.8726	0.8931	0.9009	
	$\bar{v}$	−0.0135*	0.0107	0.0514	
Re = 500	$\bar{p}$	0.9327*	1.0536	1.2570	0.9951
	$\bar{\theta}$	0.0*	0.8945	0.9067	
	$\bar{v}$	−0.0196*	−0.0166*	−0.0066*	
Re = 1000	$\bar{p}$	0.9021*	0.9172*	0.0661*	1.0043
	$\bar{\theta}$	0.0*	0.0*	0.0*	

* Negative $\bar{v}$ means that the outer pressure is greater than the inner pressure; coolant is blown inward, and the inflow temperature is given as $\bar{\theta} = 0$.

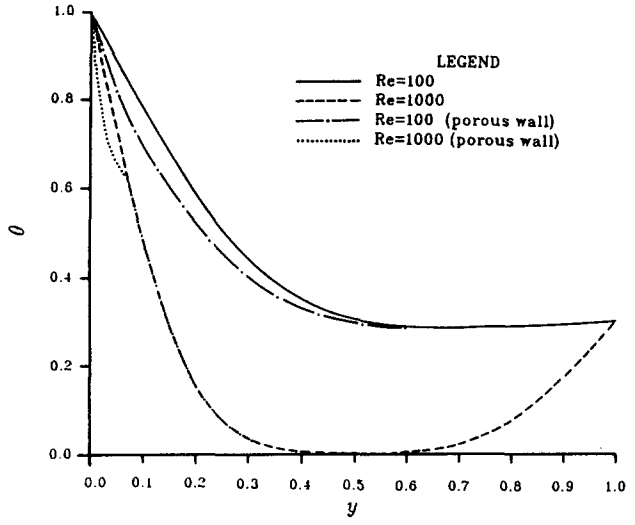

Figure 15 The θ distributions against y at $x = 8.25$ of cases where Re = 100 and 1000 with and without three porous wall segments

Equation (6) or Table 3. The total mass flow rate after the porous region, listed in the last column of Table 3, also illustrates that the suction speed decreases. In the extreme case where Re = 1000, the flow through the porous segment turns out to be a small blowing flow (see the negative $\bar{v}$ and $\theta_h = \theta_o$ in Table 3).

By inspecting Table 3, we find that $\bar{v}$ and $\bar{p}$ also drecrease as Re increases. Because a larger $\bar{v}$ (or $|\bar{p} - p_0|$) means a better heat transfer enhancement, it can be concluded that the increase of Re degenerates the heat transfer enhancement effect. For Re = 1000, only a small amount of fluid is blown into the channel, as shown in Table 3, and the heat transfer enhancement is minimal.

In engineering applications, the situation where Re $\leq$ 100 corresponds to coolant driven primarily by buoyant force. We conclude that the local heat transfer enhancement from embedding a porous wall segment in the hot wall is effective in the case of an emergence, such as when the ventilating system is inoperative. For the case of forced convection, which has a larger Re, the porous wall embedding can provide only a small local heat transfer enhancement.

Finally, we examine whether or not the thermal boundary-layer thickness is larger than the chip height ($\sim O(0.1)$). In Figure 15, the cross-sectional temperature distributions downstream of the porous wall segment ($x = 8.25$) are shown. Although the case where Re = 100 has a larger thermal boundary-layer thickness, and the case where Re = 1000 has a smaller thickness, all of them are larger than 0.1. In other words, all the situations, with or without embedded porous walls, have thermal boundary-layer thicknesses larger than the chip height.

Conclusions

Numerical simulation shows that the mixed convection heat transfer between vertical parallel plates can be enhanced locally through local suction by embedding porous wall segments on the hot wall. The position of the porous wall segment can be estimated by the numerical solution of the case with the solid wall boundary conditions. The heat transfer enhancement is a local effect and becomes more significant with increase of porosity and distance measured from the entrance. Such an enhancement is effective whenever Re $\leq$ 100, and it is less effective for a higher value of Re.

References

Aung, W., Fletcher, L. S. and Sernas, V. 1972. Developing laminar free convection between vertical flat plates with asymmetric heating. *Int. J. Heat Mass Transfer*, **15**, 2293–2308

Aung, W. and Worku, G. 1986a. Developing flow and flow reversal in a vertical channel with asymmetric wall temperature. *J. Heat Transfer*, **108**, 299–304

Aung, W. and Worku G. 1986b. Theory of fully developed combined convection including flow reversal. *J. Heat Transfer*, **108**, 485–488

Chou, J. H. and Lee, J. 1988. Reducing flow nonuniformities in LSI packages by vortex generators. *Cooling Technology for Electronic Equipment*, W. Aung, (ed.). Hemisphere, New York, 113–124

Ghia, U., Ghia, K. N. and Shin, C. T. 1982. High-Resolution for incompressible flow using the Navier–Stokes equations and a multigrid method. *J. Comp. Phys.*, **48**, 387–411

Hamed, A. and Lehnig, T. An Investigation of oblique shock/boundary layer/bleed interaction. AIAA Paper 90–1928

Hartnett, J. P. 1985. Mass transfer cooling. *Handbook of Heat Transfer*

Application, W. M. Rohsenow and J. P. Hartnett, Mc-Graw-Hill, New York, 53–101

Heaton, S. H., Reynolds, W. C. and Kays, W. M. 1964. Heat transfer in annular passages. Simultaneous development of velocity and temperature fields in laminar flow. *Int. J. Heat Mass Transfer*, **7**, 763–781

Ingham, D. B., Keen, D. J. and Heggs, P. J. 1988. Flows in vertical channels with asymmetric wall temperatures and including situations where reversal flows occur. *J. Heat Transfer*, **110**, 910–917

Jeng, Y. N. and Chen, J. L. 1992a. Truncation error analysis of the finite volume method for a model steady convective equation. *J. Comput. Phys.*, **100**, 64–72

Jeng, Y. N. and Chen, J. L. 1992b. On the geometric conservation law of the finite volume method for the SIMPLER algorithm and a proposed second-order upwind scheme, *Num. Heat Transfer. Part B*, **22**, 211–234

Jeng, Y. N., Chen, J. L. and Aung, W. 1992. On the Reynolds number independence of the mixed convection flow in a vertical channel subject to asymmetric wall temperatures with and without flow reversal, *Int. J. Heat Fluid Flow*, **13**, 329–339.

Lee, R. S. and Huang, H. C. 1988. Measuring and modeling the thermal resistance of LCCC under cooling enhancement by using turbulators. *3rd Int. Symp. on Transport Phenomena in Thermal Control*, Taipei, Taiwan, 437–447

Patera, A. T. and Mikic, B. B. 1980. Exploiting hydrodynamic instabilities, resonant heat transfer enhancement. *Int. J. Heat Mass Transfer*, **29**, 1127–1138

Payne, P. R. 1978. The theory of fabric porosity as applied to parachutes in incompressible flow. *Aeronaut. Quart.*, **29**, 175–206

Ratts, E., Amon, C. H., Mikic, B. B. and Patera, A. T. 1988. Cooling enhancement of forced convection air-cooled chip array through flow modulation induced by vortex-shedding cylinders in cross-flow. *Cooling Technology for Electronic Equipment*, W. Aung, (ed.). Hemisphere, New York, 183–194

Shyy, W. 1987. Effects of open boundary on incompressible Navier–Stokes flow computation: Numerical experiments. *Num. Heat Transfer*, **12**, 157–178

Sparrow, E. M., Chrysler, G. M. and Azevedo, L. F. 1984. Observed flow reversals and measured-predicted Nusselt numbers for natural convection in a one-sided heated vertical channel. *J. Heat Transfer*, **106**, 325–332

Sparrow, E. M., Niethemmer, J. E. and Chaboki, A. 1982. Heat transfer and pressure drop characteristic of arrays of rectangular modules encountered in electronic equipment. *Int. J. Heat Mass Transfer*, **25**, 961–973

Tao, L. N. 1960. On combined free and forced convection in channels. *J. Heat Transfer*, **82**, 233–238

Thomas, P. D. and Middlecoff, J. F. 1980. Direct control of the grid point distribution in meshes generated by elliptic equations. *AIAA J.*, **18**, 652–656